



Intrinsic superstructure near atomically clean armchair step edges of graphiteWenhan Zhang ¹, Zheng Ju,^{1,2} and Weida Wu ^{1,*}¹*Department of Physics and Astronomy, Rutgers University, Piscataway, New Jersey 08854, USA*²*Department of physics, Arizona State University, Tempe, Arizona 85287, USA*

(Received 29 June 2019; published 11 September 2019)

We investigated the electronic superstructure of a graphite surface in the vicinity of monoatomic armchair step edges with scanning tunneling microscopy and spectroscopy. Only the $(\sqrt{3} \times \sqrt{3})R30^\circ$ superstructure is visualized near atomically clean armchair edges, while the honeycomb superstructure is absent. The spectroscopic mapping near the clean armchair edge clearly reveals the $(\sqrt{3} \times \sqrt{3})R30^\circ$ superstructure on both sides of the step edge. We have also visualized a mixture of $(\sqrt{3} \times \sqrt{3})R30^\circ$ and honeycomb superstructures near structurally defective armchair edges. Our results suggest that the honeycomb superstructure pattern results from a superposition of two sets of $(\sqrt{3} \times \sqrt{3})R30^\circ$ superstructures with different phases. Our observation solves the mystery of the coexistence of two types of superstructures reported by prior studies.

DOI: [10.1103/PhysRevB.100.115120](https://doi.org/10.1103/PhysRevB.100.115120)**I. INTRODUCTION**

Graphene has drawn extensive attention in material science since its first successful isolation in 2004 [1]. The unconventional electronic properties make it a potential candidate for postsilicon electronic devices [2]. Known as a two-dimensional Dirac material, the low-energy electron excitation of graphene behaves like a massless Dirac fermion [3], which gives rise to novel electronic phenomena, such as the quantum spin Hall effect [4], Klein tunneling [5], and the anomalous quantum Hall effect [6,7]. Recently, superconductivity and magnetism were discovered in twisted bilayer graphene [8–11], which provides a new route to the development of superconducting and magnetic devices with carbon-based materials.

As the graphene is cut into nanosize fractions or semi-infinite sheets, the impact of edge on the electronic properties of graphene becomes significant [12–17]. Depending on the edge direction with respect to the lattice vector, there are two simplest types of edges, i.e., armchair and zigzag edges, as illustrated in Fig. 1. They host distinct electronic properties. Based on prior theoretical [13,14,18,19] and experimental [20–23] studies, there exists an electronic state localized on the zigzag edge of graphene due to the nonbonding π electrons of the edge carbon atoms, whereas such an edge state is absent on the armchair edge. Such enhanced local density of states (LDOS) on the zigzag edges may give rise to unusual phenomena, such as edge magnetism, which have potential for spintronics applications [24–27].

In addition, the edge also plays a role of potential barrier and induces electron wave scattering. It is manifested as a superstructure pattern, which can be directly probed by scanning tunneling microscopy. Such a superstructure pattern near the step edge on graphite has been extensively studied in the last three decades. However, there is still no consensus on the intrinsic superstructure of ideal step edges. In

the vicinity of the armchair edge, some studies show only the $(\sqrt{3} \times \sqrt{3})R30^\circ$ superstructure [20,28,29], while others report a coexistence of the $(\sqrt{3} \times \sqrt{3})R30^\circ$ and honeycomb superstructures [21,30], both of which have a characteristic wavelength of $3a/2$ ($a = 2.46 \text{ \AA}$ is the lattice constant of graphite). The $(\sqrt{3} \times \sqrt{3})R30^\circ$ superstructure is a result of electron wave scattering of intervalley K-K' ($q = 2k_F$, where k_F is the Fermi wave vector) occurring near the armchair edge. For graphite, the Fermi wave vector is located at the corner of the Brillouin zone. Therefore, the modulation of LDOS associated with the scattering wave vector q is commensurate with the underlying atomic lattice and consequently gives rise to the $(\sqrt{3} \times \sqrt{3})R30^\circ$ superstructure. On the other hand, theoretical calculations predict that there is no superstructure near the zigzag edge [21,28], while some experimental works show signatures of superstructure patterns [23,29]. These discrepancies probably originate from the structural or chemical imperfections of the edge, e.g., the mixture of armchair and zigzag edges or extrinsic adsorbates, which hinder the clear observation of intrinsic electronic properties associated with the edges [30–37].

To address this issue, we performed scanning tunneling microscopy (STM) and scanning tunneling spectroscopy (STS) experiments to study clean step edges on the surface of single-crystal graphite. This paper focuses on the armchair edge, because it is energetically more stable than the zigzag edge [38–40]. We managed to find atomically clean armchair edges on graphite as long as $\sim 30 \text{ nm}$. In the vicinity of such an edge, the $(\sqrt{3} \times \sqrt{3})R30^\circ$ superstructure is observed, while the honeycomb superstructure is absent. The STS maps measured near the armchair edge show this type of superstructure pattern on both the upper and lower terraces. Interestingly, we visualized a mixture of $(\sqrt{3} \times \sqrt{3})R30^\circ$ and honeycomb superstructures near the structurally defective armchair edge. We propose that the honeycomb superstructure pattern emerges as a superposition of two sets of $(\sqrt{3} \times \sqrt{3})R30^\circ$ superstructures at their antiphase boundary. Our observation demonstrates that the $(\sqrt{3} \times \sqrt{3})R30^\circ$ superstructure is intrinsic on the armchair step edge.

*Corresponding author: wdu@physics.rutgers.edu

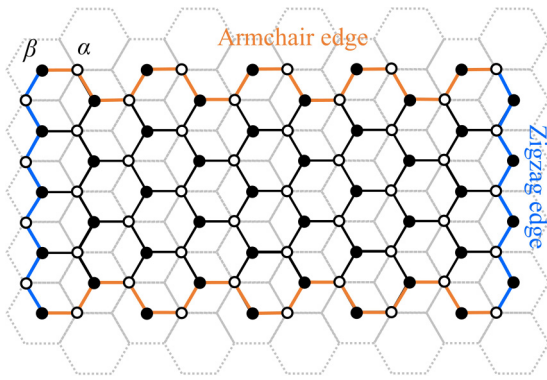


FIG. 1. Schematic of lattice structure of two atomic layers of graphite showing two types of monoatomic step edges. The black (gray) honeycomb lattice represents the upper (lower) atomic layer. The open and closed circles represent α - and β -site carbon atoms of the topmost layer. The zigzag (armchair) edges are denoted by the blue (orange) lines.

II. EXPERIMENTAL METHOD

We conducted experiments on the single crystals of highly oriented pyrolytic graphite (HOPG). The samples were cleaved *in situ* in ultrahigh vacuum ($\approx 2 \times 10^{-11}$ mbar) and then immediately transferred into the STM head for measurements. Before cleavage, they were precooled to a low temperature in the STM head, which avoids outgassing of the STM head due to a sudden rise of temperature at the moment of sample insertion and thus significantly reduces contamination on the sample surface. The STM measurements in this paper were performed at $T = 5$ K unless otherwise specified. Electrochemically etched tungsten tips as scanning probes were treated and characterized on the single-crystal Au(111) surface [41]. The STS mapping measurements were performed with the standard lock-in technique with a modulation frequency $f = 455$ Hz and a modulation amplitude $V_{\text{mod}} = 20$ mV. All the step edges of HOPG shown in this paper are monoatomic with a step height $\Delta z = 3.3$ Å.

III. RESULTS AND DISCUSSIONS

Figure 2(a) shows a topographic image near a representative step edge. Such linear step edges can extend over a few hundred nanometers. In the area far from the edge, the intrinsic lattice of the topmost layer of graphite is observed, as shown in Fig. 2(b). The atomic corrugation is the most pronounced at low sample bias (+0.2 eV) and shows a hexagonal lattice. A phase shift of $2\pi/3$ of such a lattice across the step edge indicates that the resolved carbon atoms are at the β site, i.e., there are no carbon atoms directly below or above in adjacent layers (see the Appendix for detailed phase analysis). This is consistent with previous STM studies [42]. With the atomic resolution, the step edge in Fig. 2(a) can be identified as an armchair step edge, because it is perpendicular to the atomic row of β -site carbon atoms. The most common monoatomic step edges are armchair step edges in our measurements. We did not observe linear zigzag edges on naturally cleaved HOPG surfaces. Due to the low- T cleavage, the edge is partially clean. The bright spots marked by red

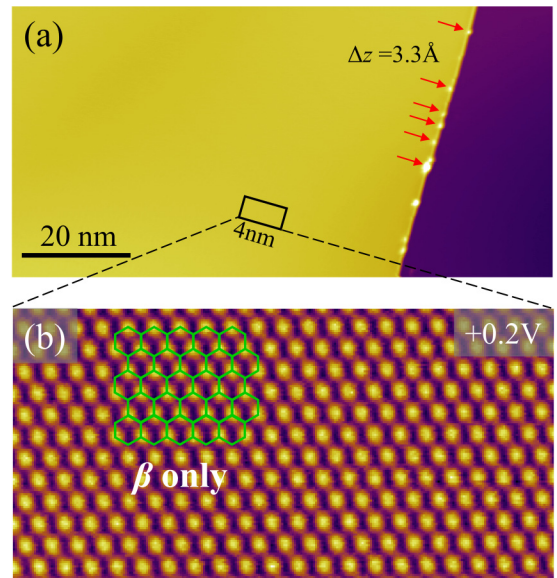


FIG. 2. (a) Large-scale topographic image containing an armchair step edge. The red arrows mark representative imperfections such as adsorbates on the edge. Tunneling condition: $I = 100$ pA, $V = -1$ V. (b) Atomically resolved topographic image taken far from the edge showing the intrinsic lattice structure of the graphene sheet. Tunneling condition: $I = 1$ nA, $V = +0.2$ V. The green honeycomb lattice shows the atomic lattice. Only β -site carbon atoms are observed.

arrows are likely adsorbates on the edge, and the straight segments between them are clean and homogeneous.

In Fig. 3, we present atomically resolved topographic images measured in the upper terraces near clean and homogeneous segments of the armchair edge, which reveals that the $(\sqrt{3} \times \sqrt{3})R30^\circ$ superstructure is intrinsic to the armchair step edge of graphite. Figure 3(a) shows a typical region containing a clean part of the armchair edge taken at +0.2 V. The color scale is adjusted to highlight the atomic corrugation on the upper terrace. Clearly, only the $(\sqrt{3} \times \sqrt{3})R30^\circ$ superstructure is visualized, as denoted by the green rhombuses. In Fig. 3(b), the line profile taken along an atomic row of the β site [red line in Fig. 2(a)] shows that the apparent heights of three adjacent β -site atoms are all different, which further substantiates the existence of the $(\sqrt{3} \times \sqrt{3})R30^\circ$ superstructure. The superstructure extends over 6–7 nm from the edge. Figures 3(c) and 3(d) show the detailed atomic lattice on the edge. Among the outermost carbon atoms, those at the β site appear as bright spots. In contrast, the α -site atoms are not visible. The uniqueness of the β -site atoms on the edge probably results from the existence of dangling bonds at β sites, as there are no carbon atoms in the adjacent layers that are aligned with them in the z direction.

The $(\sqrt{3} \times \sqrt{3})R30^\circ$ superstructure being intrinsic to the clean and homogeneous armchair edge is reproduced on multiple samples and robust to an elevated temperature as high as 48 K. Figure 3(e) shows a long clean armchair edge on the surface of a new piece of HOPG (denoted as Sample 2). The atomically resolved topographic image in Fig. 3(g) indicates that the clear $(\sqrt{3} \times \sqrt{3})R30^\circ$ superstructure pattern extends over ~ 20 nm along the edge. A third HOPG sample (Sample

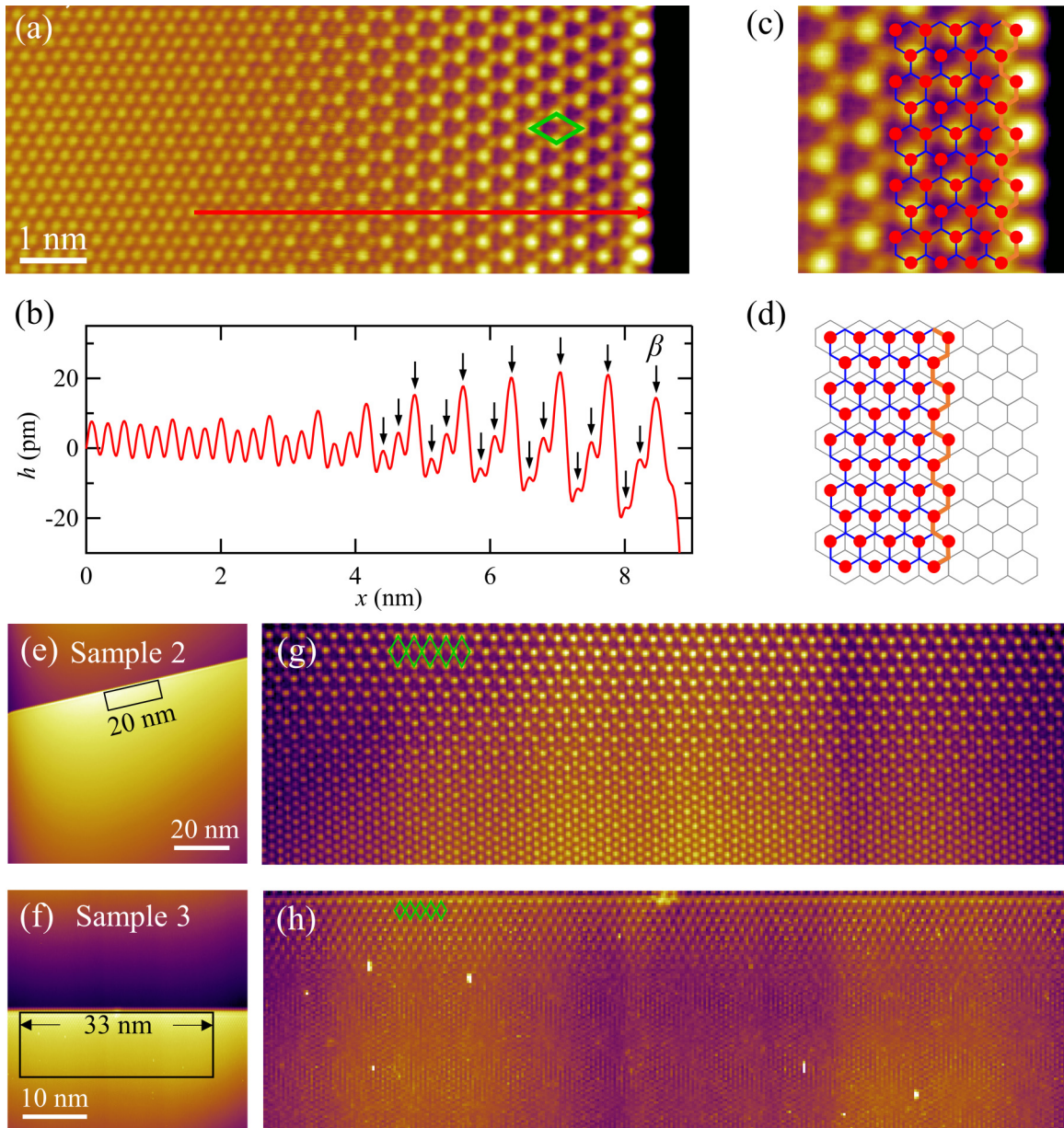


FIG. 3. (a) Topographic image taken near a clean armchair edge. The $(\sqrt{3} \times \sqrt{3})R30^\circ$ superstructure is observed in this area, as marked by the green rhombus. Tunneling condition: $I = 1$ nA, $V = +0.2$ V. (b) Line profile taken along an atomic row of the β site marked by the red line in panel (a). The atomic corrugation of β -site carbon atoms is marked by black arrows. (c) Zoom-in topographic image on the upper terrace of the armchair edge, where the atomic sites are specified by the schematic. The red dots represent the β -site carbon atoms. (d) The atomic lattice of the armchair edge. (e, f) Homogeneous armchair edges observed on different samples: (e) $I = 10$ pA, $V = -1$ V and (f) $I = 0.1$ nA, $V = -1$ V. (g, h) Zoom-in topographic images of upper terraces of the edges shown in panels (e) and (f): (g) $I = 0.1$ nA, $V = +0.2$ V and (h) $I = 0.1$ nA, $V = -0.2$ V. The $(\sqrt{3} \times \sqrt{3})R30^\circ$ superstructure extends over 30 nm along the edge without interruption. The green rhombuses mark the unit cells of the superstructure.

3) was cleaved and measured at ~ 48 K. Similarly, near the defectless armchair edge, the $(\sqrt{3} \times \sqrt{3})R30^\circ$ superstructure pattern persists longer than 30 nm along the edge, as shown in Figs. 3(f) and 3(h). In all these cases, no honeycomb superstructure is observed near clean and homogeneous armchair edges.

Our STS results obtained in the vicinity of armchair edges reveal that the superstructure observed in the topographic images originates from the unusual spatial distribution of LDOS. Figure 4(a) shows a topographic image in the same

area as in Fig. 3(a). The color scale of the lower terrace (the right side) of the edge is adjusted, so that the β -site carbon atoms in this area are also visible. As shown, they present a hexagonal lattice without clear superstructure patterns. Figure 4(b) shows the typical individual dI/dV spectra taken at selective locations. The red dI/dV spectra were measured on top of pronounced β -site atoms near the edge [marked by red arrows in Fig. 4(a)]. It has higher LDOS at positive bias compared with the gray curve taken in the normal region far from the edge. This is possibly due to the positive interference

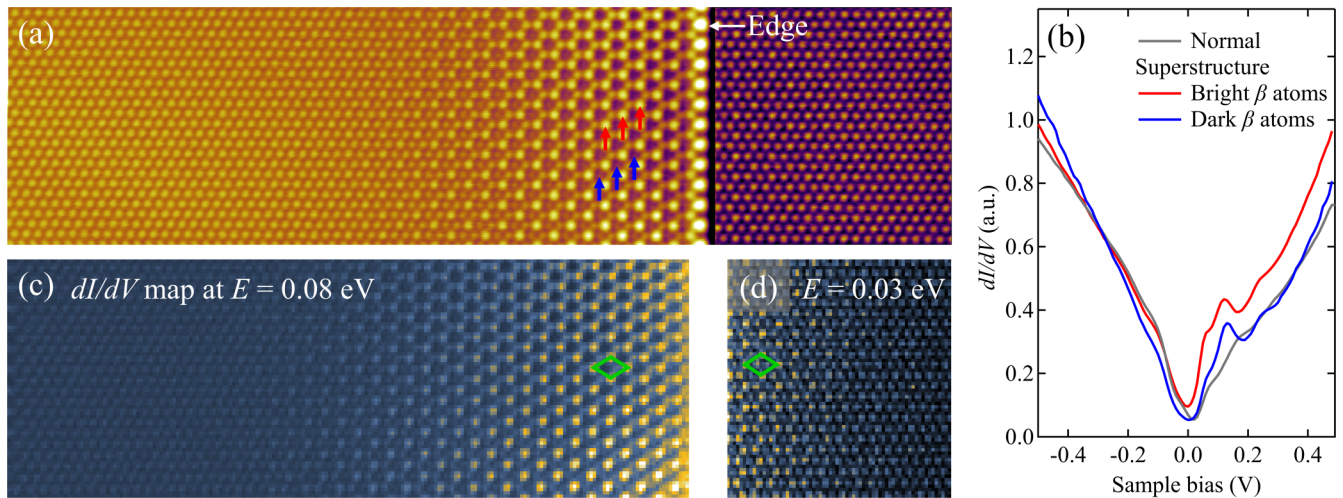


FIG. 4. (a) Topographic image taken in the same area of Fig. 3(b). Tunneling condition: $I = 1$ nA, $V = +0.2$ V. No superstructure is observed in the lower terrace (right). (b) Individual dI/dV spectra taken in different areas. (c, d) dI/dV maps taken on the upper and lower areas, respectively.

of plane waves from the potential barrier created by the edge. The presence of the superstructure is characterized by the LDOS contrast between the pronounced atoms and the faint atoms at the β site [marked by the blue arrows in Fig. 4(a)]. The individual dI/dV spectrum on pronounced atoms (red curve) has higher intensity within $(-0.27$ eV, $+0.5$ eV) and lower intensity within $(-0.5$ eV, -0.27 eV) than that on faint atoms (blue curve), which suggests the superstructure would influence the electronic structure over a wide energy range. Indeed, our STS imaging measurement on the upper terrace of the edge shows a $(\sqrt{3} \times \sqrt{3})R30^\circ$ superstructure pattern from -0.5 to 0.5 eV except at around -0.27 eV (see Supplemental Material [43]). Across -0.27 eV, a phase shift of the superstructure is observed, where the bright atoms become dark and vice versa. Consistently, the dI/dV spectra taken on two types of β -site atoms in Fig. 4(b) intersect at that energy. Figure 4(c) shows an exemplary dI/dV map at $+0.08$ eV, where the superstructure pattern clearly appears. To our surprise, the superstructure pattern can also be observed in the dI/dV map of the lower terrace, although it is much weaker than that on the upper terrace, as demonstrated in Fig. 4(d). It indicates that the potential barrier created by the step edge has a weaker influence on the electronic properties of electrons on the lower atomic layer. To our knowledge, the superstructure has never been observed on the lower terrace below the step edge in the prior reports. Another feature appearing in the dI/dV spectra is a LDOS peak at ~ 0.12 eV above the Fermi level (E_F) emerging in the superstructure region. This feature is reproducible near the different edges on multiple samples, and is consistent with prior STM studies [21].

To quantitatively study the intensity of superstructure patterns in the STS results, we performed Fourier transform (FT) on the dI/dV maps. Figures 5(a) and 5(b) show the FT of dI/dV maps shown in Figs. 4(c) and 4(d). The outer six peaks correspond to the fundamental hexagonal lattice of β -site atoms. The inner six peaks marked by the red and blue arrows correspond to the $(\sqrt{3} \times \sqrt{3})R30^\circ$ superstructure patterns. Figure 5(c) plots the intensities of superstructure peaks as

functions of the energy. On the upper terrace of the edge, the peak intensity of the superstructure is larger than zero in the whole energy range of $(-0.5$ eV, $+0.5$ eV) except a small energy interval around -0.27 eV, which is consistent with our direct observation in the dI/dV map. On the other hand, the peak intensity of the superstructure on the lower terrace takes a nonzero value only in a narrower energy range $(0, +0.4$ eV) and it is much weaker compared to that on the upper terrace. Note that its highest value at $+0.03$ eV is ~ 25 times smaller than that on the upper terrace at 0.08 eV. Such a small ratio is consistent with the much weaker interlayer hopping energy compared to the intraplane hopping energy [2]. Because there

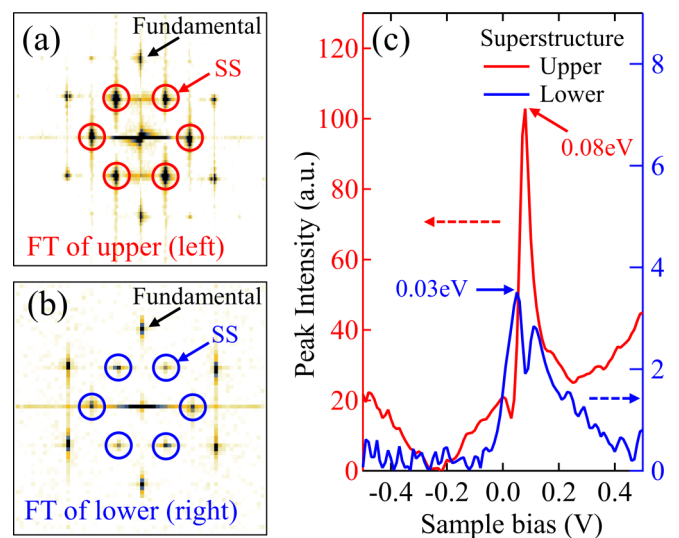


FIG. 5. (a) FT of the dI/dV map in Fig. 4(c). The corresponding energy is $E = 0.08$ eV, at which the superstructure (SS) is the most pronounced on the upper terrace. (b) FT of the dI/dV map in Fig. 4(d). The corresponding energy is $E = 0.03$ eV, at which the superstructure is the most pronounced on the lower terrace. (c) The intensities of SS peaks in FT maps in panels (a) and (b) as functions of the energy.

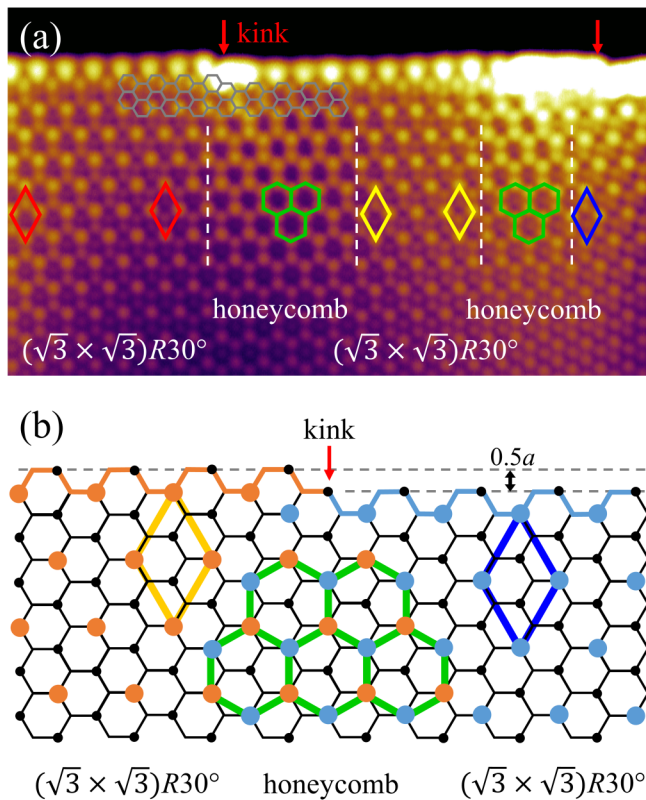


FIG. 6. (a) Topographic image of the armchair step edge with a mixture of the $(\sqrt{3} \times \sqrt{3})R30^\circ$ and honeycomb superstructures. Tunneling condition: $I = 1$ nA, $V = +0.2$ V. The rhombuses and honeycombs illustrate the superstructures. The honeycomb superstructure is due to overlap of two sets of intrinsic $(\sqrt{3} \times \sqrt{3})R30^\circ$ superstructures with a phase shift. (c) Lattice structure showing that the honeycomb superstructure emerges in the middle of armchair edges with a lattice offset. It is a result of overlapping of two sets of $(\sqrt{3} \times \sqrt{3})R30^\circ$ superstructures with a phase difference.

is no physical boundary in the lower terrace, the electrons “feel” the scattering potential created by the step edge on the upper terrace via interlayer hopping, which is much weaker than intralayer hopping. Thus, the scattering probability on the lower terrace is much weaker than that of the upper terrace, resulting in much weaker superstructure modulation.

So far, our experiments have revealed that only the $(\sqrt{3} \times \sqrt{3})R30^\circ$ superstructure emerges near the linear and defectless monoatomic armchair step edge, while no honeycomb superstructure is observed in the vicinity of such an edge. However, we found that the honeycomb superstructure can exist if the armchair edge is not perfectly straight. In the region shown in Fig. 6(a), there are two kinks on the edge marked by the red arrows. As demonstrated by the gray mesh of honeycomb lattice, each kink is a very short zigzag edge located at the boundary of two fragments of armchair edge. The atomic row of terminating carbon atoms on the two sides of the kink has an offset of half the lattice constant perpendicular to the edge. The atomic lattice near the kinks is not perfectly linear, possibly because of the strain effect on the edge carbon atoms. Interestingly, the $(\sqrt{3} \times \sqrt{3})R30^\circ$ and honeycomb superstructures emerge alternatively, as demonstrated by the colorful rhombuses and honeycombs in Fig. 6(a)

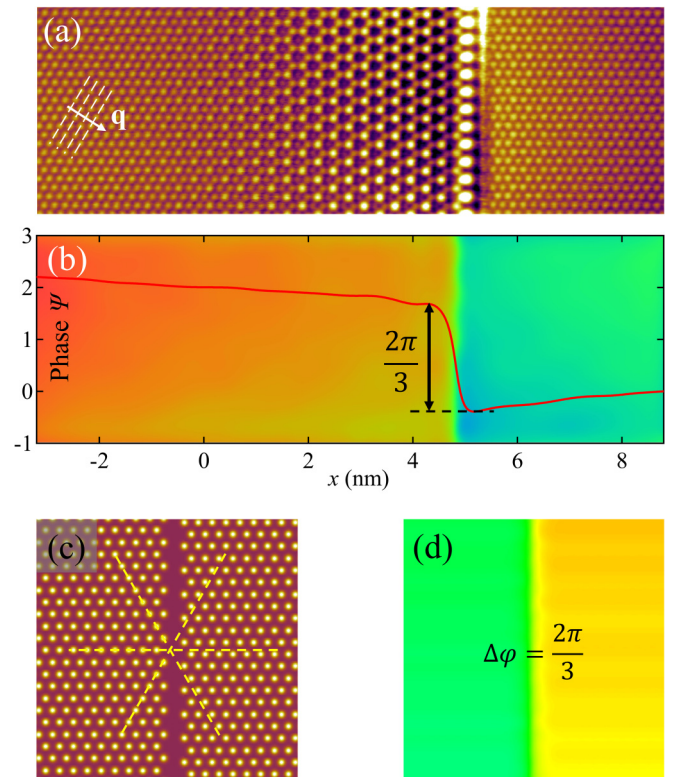


FIG. 7. (a) Topographic image across the armchair edge, which is taken in the same area as in Fig. 3(a). Tunneling condition: $I = 1$ nA, $V = +0.2$ V. \mathbf{q} marks the direction in which the phase of the lattice is calculated. (b) Phase map and line profile of the phase taken perpendicular to the edge. The phase difference between the upper and lower terraces is $2\pi/3$. (c) Ideal hexagonal lattice with a phase shift of $2\pi/3$ at the antiphase boundary that simulates the β -site carbon atoms of two adjacent layers. (d) Corresponding phase map of panel (c).

as a guide to the eye. Note that right under a homogeneous part of the armchair edge is always the $(\sqrt{3} \times \sqrt{3})R30^\circ$ superstructure, while the honeycomb superstructure is visible near the kink between two parts of the armchair edge. Herein the coexistence of the two different types of superstructures can be understood phenomenologically as follows. In the case that a kink separates two segments of the armchair edge with an offset of an atomic row, each part of the armchair edge gives rise to an interference pattern (orange and blue dots) manifested as the $(\sqrt{3} \times \sqrt{3})R30^\circ$ superstructure (blue and orange rhombuses). With the equivalent apparent height at the antiphase boundary, the superposition of the two superstructure patterns creates a honeycomb superstructure (large green honeycomb), as illustrated in Fig. 6(b).

These kinks are not rare along the edge in a large scale. If the step edge of graphite or the edge of graphene is not clean or atomically smooth, it is very challenging to identify these structural imperfections with lack of clear atomic resolution in the vicinity of the edge. With many kinks, a visually straight armchair edge can still give rise to a coexistence of two types of superstructures, as demonstrated in Fig. 6. In addition to the structural imperfection, chemical imperfection such as adsorbates may also contribute to the creation of a more

complicated superstructure. Future studies will address this issue.

IV. CONCLUSION

In summary, our experiments reveal that the $(\sqrt{3} \times \sqrt{3})R30^\circ$ superstructure is the intrinsic superperiodic pattern of the clean and ideal armchair step edge of graphite. We visualized the $(\sqrt{3} \times \sqrt{3})R30^\circ$ superstructure not only on the upper terrace but also on the lower terrace, which indicates the electronic influence of the step edge as a potential barrier on both the first and the second atomic layers. The honeycomb superstructure sandwiched by the $(\sqrt{3} \times \sqrt{3})R30^\circ$ superstructure is also observed near a structural imperfection that separates two parts of armchair edge with an offset. Such a honeycomb superstructure can be viewed as a superposition of two sets of intrinsic $(\sqrt{3} \times \sqrt{3})R30^\circ$ superstructures. This finding reconciles the different experimental observations about superstructure patterns in prior STM studies.

ACKNOWLEDGMENTS

We thank Jixia Dai and Chen Chen for helpful discussions. This work was supported by NSF Grant No. DMR-1506618.

APPENDIX: IDENTIFICATION OF β -SITE CARBON ATOMS VIA PHASE ANALYSIS

Via quantitative analysis, we confirm that the hexagonal lattice visualized in the topographic image taken at +0.2 eV is composed of β -site carbon atoms. The atomic row can be regarded as a plane wave in the direction of the reciprocal-lattice vector with a magnitude $q = 2\pi/d$, where d is the distance between two adjacent atomic rows, as demonstrated in Fig. 7(a). The direction and magnitude of q can be accurately obtained in the FT of the topographic image. The local phase of the lattice associated with q in the real space can then be extracted through FT analysis [44]. The lattices of the α sites of two adjacent layers have the same phase, because they overlap in the z direction. In contrast, the lattices of the β sites of two adjacent layers are not aligned with each other, and have a phase difference of $2\pi/3$. As shown by the phase map and line profile of the phase in Fig. 7(b), the lattices on the two sides of the edge show a phase shift of $\Delta\phi = 2\pi/3$, which indicates the atoms visualized are at the β site. We also simulated the ideal β -site atomic lattices of two adjacent layers of graphite and calculated the phase map with the same analysis. As shown in Figs. 7(c) and 7(d), the phase shift across the antiphase boundary equals $2\pi/3$, which agrees with our experimental results.

-
- [1] K. S. Novoselov, *Science* **306**, 666 (2004).
 [2] A. H. Castro Neto, F. Guinea, N. M. R. Peres, K. S. Novoselov, and A. K. Geim, *Rev. Mod. Phys.* **81**, 109 (2009).
 [3] T. Wehling, A. Black-Schaffer, and A. Balatsky, *Adv. Phys.* **63**, 1 (2014).
 [4] C. L. Kane and E. J. Mele, *Phys. Rev. Lett.* **95**, 226801 (2005).
 [5] C. W. J. Beenakker, *Rev. Mod. Phys.* **80**, 1337 (2008).
 [6] K. S. Novoselov, A. K. Geim, S. V. Morozov, D. Jiang, M. I. Katsnelson, I. V. Grigorieva, S. V. Dubonos, and A. A. Firsov, *Nature (London)* **438**, 197 (2005).
 [7] Y. Zhang, Y.-W. Tan, H. L. Stormer, and P. Kim, *Nature (London)* **438**, 201 (2005).
 [8] Y. Cao, V. Fatemi, S. Fang, K. Watanabe, T. Taniguchi, E. Kaxiras, and P. Jarillo-Herrero, *Nature (London)* **556**, 43 (2018).
 [9] M. Yankowitz, S. Chen, H. Polshyn, Y. Zhang, K. Watanabe, T. Taniguchi, D. Graf, A. F. Young, and C. R. Dean, *Science* **363**, 1059 (2019).
 [10] G. Tarnopolsky, A. J. Kruchkov, and A. Vishwanath, *Phys. Rev. Lett.* **122**, 106405 (2019).
 [11] A. L. Sharpe, E. J. Fox, A. W. Barnard, J. Finney, K. Watanabe, T. Taniguchi, M. A. Kastner, and D. Goldhaber-Gordon, *Science* **365**, 605 (2019).
 [12] S. E. Stein and R. L. Brown, *J. Am. Chem. Soc.* **109**, 3721 (1987).
 [13] M. Fujita, K. Wakabayashi, K. Nakada, and K. Kusakabe, *J. Phys. Soc. Jpn.* **65**, 1920 (1996).
 [14] K. Nakada, M. Fujita, G. Dresselhaus, and M. S. Dresselhaus, *Phys. Rev. B* **54**, 17954 (1996).
 [15] A. Affoune, B. Prasad, H. Sato, T. Enoki, Y. Kaburagi, and Y. Hishiyama, *Chem. Phys. Lett.* **348**, 17 (2001).
 [16] L. G. Cançado, M. A. Pimenta, B. R. A. Neves, G. Medeiros-Ribeiro, T. Enoki, Y. Kobayashi, K. Takai, K.-i. Fukui, M. S. Dresselhaus, R. Saito, and A. Jorio, *Phys. Rev. Lett.* **93**, 047403 (2004).
 [17] T. Enoki, *Phys. Scr. T* **146**, 014008 (2012).
 [18] L. Brey and H. A. Fertig, *Phys. Rev. B* **73**, 235411 (2006).
 [19] A. R. Akhmerov and C. W. J. Beenakker, *Phys. Rev. B* **77**, 085423 (2008).
 [20] Y. Kobayashi, K.-i. Fukui, T. Enoki, and K. Kusakabe, *Phys. Rev. B* **73**, 125415 (2006).
 [21] Y. Niimi, T. Matsui, H. Kambara, K. Tagami, M. Tsukada, and H. Fukuyama, *Phys. Rev. B* **73**, 085421 (2006).
 [22] C. Tao, L. Jiao, O. V. Yazyev, Y.-C. Chen, J. Feng, X. Zhang, R. B. Capaz, J. M. Tour, A. Zettl, S. G. Louie, H. Dai, and M. F. Crommie, *Nat. Phys.* **7**, 616 (2011).
 [23] M. Ziatdinov, S. Fujii, K. Kusakabe, M. Kiguchi, T. Mori, and T. Enoki, *Phys. Rev. B* **87**, 115427 (2013).
 [24] K. Kusakabe and M. Maruyama, *Phys. Rev. B* **67**, 092406 (2003).
 [25] H. Lee, Y.-W. Son, N. Park, S. Han, and J. Yu, *Phys. Rev. B* **72**, 174431 (2005).
 [26] Y.-W. Son, M. L. Cohen, and S. G. Louie, *Nature (London)* **444**, 347 (2006).
 [27] O. V. Yazyev and M. I. Katsnelson, *Phys. Rev. Lett.* **100**, 047209 (2008).
 [28] P. L. Giunta and S. P. Kelty, *J. Chem. Phys.* **114**, 1807 (2001).
 [29] Y. Kobayashi, K.-i. Fukui, T. Enoki, K. Kusakabe, and Y. Kaburagi, *Phys. Rev. B* **71**, 193406 (2005).
 [30] K.-i. Sakai, K. Takai, K.-i. Fukui, T. Nakanishi, and T. Enoki, *Phys. Rev. B* **81**, 235417 (2010).

- [31] H. A. Mizes and J. S. Foster, *Science* **244**, 559 (1989).
- [32] J. Xhie, K. Sattler, U. Müller, N. Venkateswaran, and G. Raina, *Phys. Rev. B* **43**, 8917 (1991).
- [33] G. Shedd and P. Russell, *Surf. Sci.* **266**, 259 (1992).
- [34] J. Valenzuela-Benavides and L. Morales de la Garza, *Surf. Sci.* **330**, 227 (1995).
- [35] P. Ruffieux, O. Gröning, P. Schwaller, L. Schlapbach, and P. Gröning, *Phys. Rev. Lett.* **84**, 4910 (2000).
- [36] J. M. López, M. Passeggi, and J. Ferrón, *Surf. Sci.* **602**, 671 (2008).
- [37] M. Ziatdinov, S. Fujii, K. Kusakabe, M. Kiguchi, T. Mori, and T. Enoki, *Phys. Rev. B* **89**, 155405 (2014).
- [38] Y. H. Lee, S. G. Kim, and D. Tománek, *Phys. Rev. Lett.* **78**, 2393 (1997).
- [39] T. Kawai, Y. Miyamoto, O. Sugino, and Y. Koga, *Phys. Rev. B* **62**, R16349 (2000).
- [40] S. Okada, *Phys. Rev. B* **77**, 041408(R) (2008).
- [41] W. Chen, V. Madhavan, T. Jamneala, and M. F. Crommie, *Phys. Rev. Lett.* **80**, 1469 (1998).
- [42] S. Gwo and C. K. Shih, *Phys. Rev. B* **47**, 13059 (1993).
- [43] See Supplemental Material at <http://link.aps.org/supplemental/10.1103/PhysRevB.100.115120> for the STS mapping results.
- [44] M. J. Lawler, K. Fujita, J. Lee, A. R. Schmidt, Y. Kohsaka, C. K. Kim, H. Eisaki, S. Uchida, J. C. Davis, J. P. Sethna, and E.-A. Kim, *Nature (London)* **466**, 347 (2010).